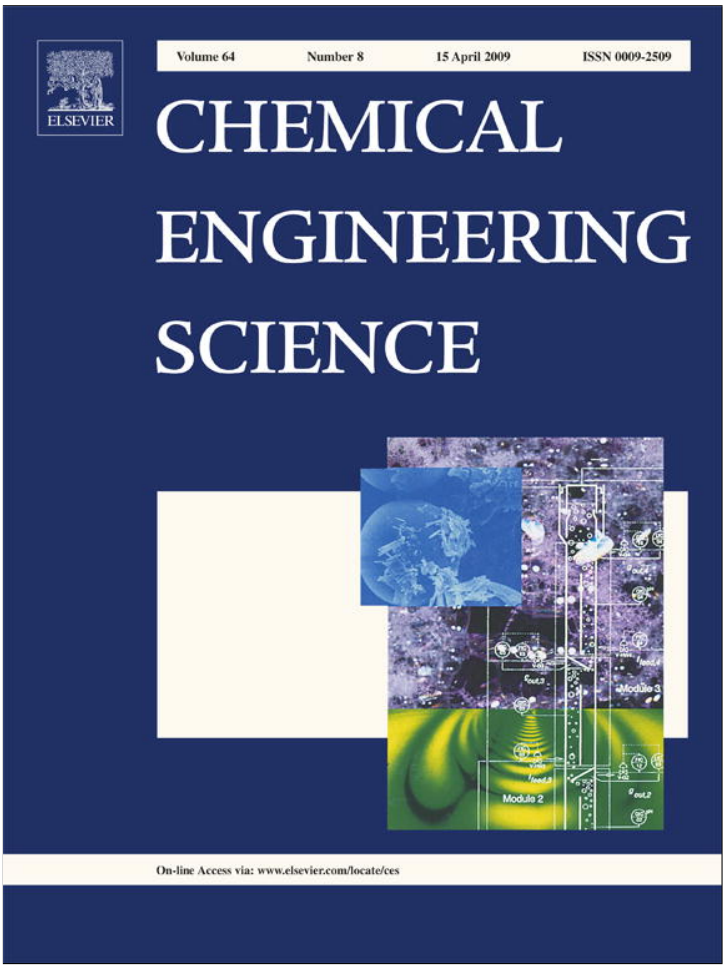

Chemical Engineering Science 64 (2009) 1747 – 1758

Contents lists available at ScienceDirect

Chemical Engineering Science

journal homepage: www.elsevier.com/locate/ces

Comparison of steric effects in the modeling of spheres and rodlike particles in field-flow fractionation☆

Frederick R. Phelan Jr.*, Barry J. Bauer

Polymers Division, NIST, Gaithersburg, MD 20899, USA

ARTICLE INFO

Article history:
Received 17 April 2008
Received in revised form 30 September 2008
Accepted 3 October 2008
Available online 19 October 2008

Keywords:
Separations
Complex fluids
Fluid mechanics
Hydrodynamics
Mathematical modelling
Simulation
Brownian dynamics
Field-flow fractionation
Nanotubes
Steric inversion
SWNTs

ABSTRACT

The elution of spheres and rods in field-flow fractionation (FFF) is studied using a Brownian dynamics method. The particle motions for spheres are governed by a familiar Langevin equation which models drag force and diffusion. The rods are modeled as prolate ellipsoids and the particle motions are governed by a similar but orientation dependent Langevin equation, and the Jeffrey equation with rotational diffusion. Modeling of particle elution for spheres from 10 to 1000 nm was examined. The simulation captures the steric transition, and results for mean elution time are in good agreement with the steric inversion theory of Giddings [Giddings, J.C., 2000. In: Field-Flow Fractionation Handbook, Wiley-Interscience; Giddings, J.C., 1978. Separation Science and Technology 13, 241; Giddings, J.C., Myers, M.N., 1978. Separation Science and Technology 13, 637]. The sphere simulations are compared with simulations for rods of equal diffusivity, as under "normal mode" conditions (i.e., diffusion controlled) such particles should elute at the same rate. The results for rods show that nanotube size particles elute by a normal mode mechanism up to a size of about 500 nm (based on a particle diameter of 1 nm). At larger sizes, the rods begin to deviate from normal mode theory, but less strongly and in the opposite sense as for spheres. While the steric effect for spheres causes larger spheres to elute faster than predicted by normal mode theory, an inverse steric effect occurs for rods in which larger rods move increasingly slower than predicted by theory. The difference is attributed to the fact that the speed up observed for spheres is dictated by size exclusion of the particles at the boundary, while rods slow down due to increasing alignment at the boundary. Spheres and rods of equivalent diffusivity elute at the same rate up to a sphere size of approximately 90 nm (500 nm rods), at which point there are increasingly greater differences in mean elution times. While this affects the calibration of such operations, it also indicates that length based separations for nanotubes are not bound by the same limitation as occurs for spheres due to steric inversion.

Published by Elsevier Ltd.

1. Introduction

Field-flow fractionation (FFF) (Giddings, 1993, 2000; Janca, 1987) is a technique for separating colloidal, macromolecular, and particulate materials ranging from 10^{-3} to 10^{2} μm in size and has recently been applied to the separation of nanotubes (Chen and Selegue, 2002; Moon et al., 2004; Selegue et al., 2001; Tagmatarchis et al., 2005; Peng et al., 2006; Liu et al., 1998; Chun et al., 2008). In FFF, a mixture to be separated is driven through a channel while a field force is applied perpendicular to the streamwise flow. The perpendicular field may be a second flow field, an electric field, or a temperature gradient, amongst a number of possibilities. The field is chosen so that the interaction between the field and the streamwise parabolic velocity profile promotes a separation of components based on their relative mobility in the field.

Rectangular frit inlet symmetrical, FFF (RSF^4), one of the variations of classical flow-FFF, is shown in Fig. 1. The mixture to be separated is injected into the channel and a cross flow is imposed upon the throughput flow driving the particulates towards the lower boundary (called accumulation wall). The cross flow is achieved through the use of porous membranes that allow solvent flow, but which are impermeable to the particles. The flow rates in the throughput and cross flow directions are independently varied by means of pressure controllers to manipulate the rate at which particles traverse the system, and to control how closely particles of different size approach the accumulation wall (without embedding). Separation is achieved due to the different residence times of the particles based upon their average equilibrium position in the parabolic velocity profile. Particles that travel on average

☆Official contribution of the National Institute of Standards and Technology; not subject to copyright in the United States.

* Corresponding author.
E-mail address: frederick.phelan@nist.gov (Frederick R. Phelan Jr).

0009-2509/$ - see front matter Published by Elsevier Ltd.
doi:10.1016/j.ces.2008.10.006

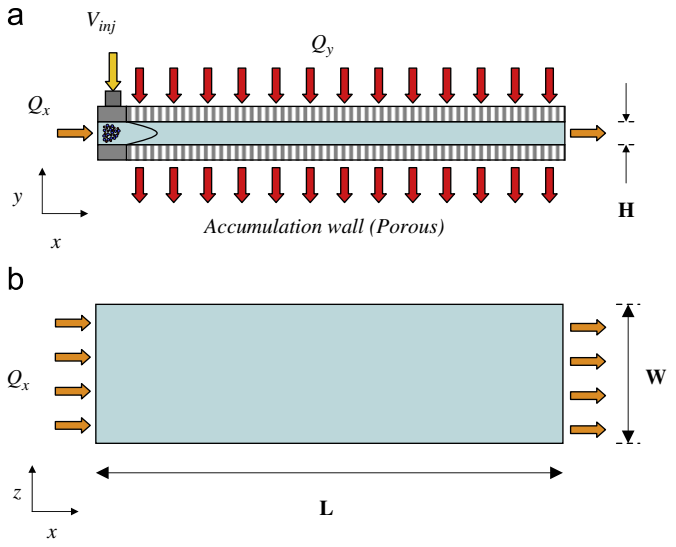

Fig. 1. (a) Side view and (b) top view, of frit inlet symmetrical, field-flow fractionation (RSF[4]). The device has a length L, thickness H, and width W. The flowrates in the x- and y-directions are independently controlled.

closer to the center elute more quickly than those that travel more closely to the wall. In practice, the length, L, of the flow channel is much greater than the gap width, H. Gap widths on the order of 100–500 μm are typically used although gaps as small as 10 μm have also been reported (Giddings, 1993). The process may be optimized in a number of ways. The throughput channel may be tapered in the third direction to further accelerate faster moving particles in a configuration called trapezoidal FFF (TAF[4]). Programmable cross flow rates can go to zero through a ramp or step function to allow slower moving particles to elute more quickly once fast movers have exited. The accumulation wall may be constructed of different materials to influence the separation by promoting different types of interactions with the particles (Song et al., 2003).

A number of different mechanisms can be exploited to achieve separation in flow-FFF (Giddings, 1993, 2000; Janca, 1987). What is termed "normal mode" separation applies to particles that are small enough to undergo significant Brownian motion and whose size is negligible compared to the thickness of the channel. Because the solutions are dilute (i.e., hydrodynamic interactions are negligible), the main forces acting on the particles are the viscous drag force and the Brownian force. Under these conditions, smaller particles which are more diffusive, travel with an average position closer to the centerline and elute more quickly than larger particles, as depicted in the upper part of Fig. 2a. For an ensemble of particles, the competition between advection and diffusion in the cross flow direction drives particles of different sizes to distinct average positions. The particle "clouds" are characterized by their average horizontal spread along the throughput direction, Δx, and their average position from the accumulation wall, Δy, as depicted in Fig. 2a. Clean separation between different components is achieved when particle clouds of different type do not overlap, and hence, a separation distance d is achieved between the horizontal positions of the layers.

A second mechanism for separation in flow-FFF is called "steric mode" and is driven by size exclusion at the boundary. Steric mode occurs when the particle layer in FFF is strongly compressed to a thin layer at or right above the accumulation wall, as depicted in Fig. 2b. This occurs when diffusion is either negligible (based on size) or strongly suppressed by a high cross flow. In this case, larger particles are more highly entrained by the throughput flow than smaller ones (see the upper part of Fig. 2b), and thus, in steric mode large particles elute more quickly. Because diffusion effects are suppressed in steric mode separations, the horizontal spread of the particles is less than that seen in normal mode and the separation peaks are sharper. The process by which normal mode FFF begins to change over to steric mode FFF due to increasing particle diameter is called steric inversion. Steric inversion is identified by a maximum in the average elution time vs. particle size plots.

The separation process in flow-FFF is characterized by the theoretical variable called the retention, R, which is given by

$$R = \frac{\overline{U}}{\bar{u}} = \frac{\langle c(y)u(y)\rangle}{\langle c(y)\rangle\langle u(y)\rangle} \tag{1.1}$$

where $\overline{U}$ is the average streamwise velocity of the solute, c is the concentration of the solute, $\bar{u}$ is the average streamwise velocity of the carrier fluid, and the brackets $\langle\ldots\rangle$ represent the integral average over the flow cross section. The retention is a dimensionless variable whose value is bounded in the range $0 < R < 1$. The significance of the retention is that it represents the ratio of the average residence time of non-retained tracers, t_0, to the average retention time of the particles, t_r, *viz.*

$$\frac{t_r}{t_0} = \frac{1}{R} \tag{1.2}$$

where $t_0 = L/\bar{u}$ and L is the device length in the throughput direction. In the limit $R = 0$, particles are trapped on the accumulation wall, and this corresponds to the case of zero elution. As R increases, the average speed at which particles elute also increases approaching the solvent time t_0 at $R = 1$. Thus, the ability to separate particles can be compared based on the relative retention values of the different particles dispersed in the solution.

A number of analytical expressions for the retention have been developed in the literature. For RSF[4], under normal mode conditions, the competition between advection and diffusion in the cross flow direction leads particles to an equilibrium concentration profile in the gap direction given by (Giddings, 1993, 2000; Janca, 1987)

$$\frac{c}{c_0} = \exp\left(-\frac{y}{\ell}\right) \tag{1.3}$$

where c_0 is the concentration of the particles at the accumulation wall, ℓ is a characteristic length given by

$$\ell = \frac{D}{|v_c|} \tag{1.4}$$

v_c is the cross flow velocity and D is the diffusion coefficient of the particle in the cross flow direction. Assuming a parabolic velocity profile for flow in the throughput direction and that the value for $|v_c|$ is constant, Eq. (1.1) can be integrated to yield an analytical relation for the retention given by

$$R = 6\lambda\left[\coth\left(\frac{1}{2\lambda}\right) - 2\lambda\right] \tag{1.5}$$

where λ is an inverse Peclet Number (Pe) given by

$$\lambda = \frac{D}{|v_c|H} = \frac{1}{Pe} \tag{1.6}$$

For $\lambda \ll 1$, the retention has the asymptotic value

$$\lim_{\lambda\to 0} R = 6\lambda \tag{1.7}$$

Because the only specific particle property the retention depends on is the diffusion coefficient, Eq. (1.5) indicates that particles of different shape but equal diffusivity should elute at the same rate.

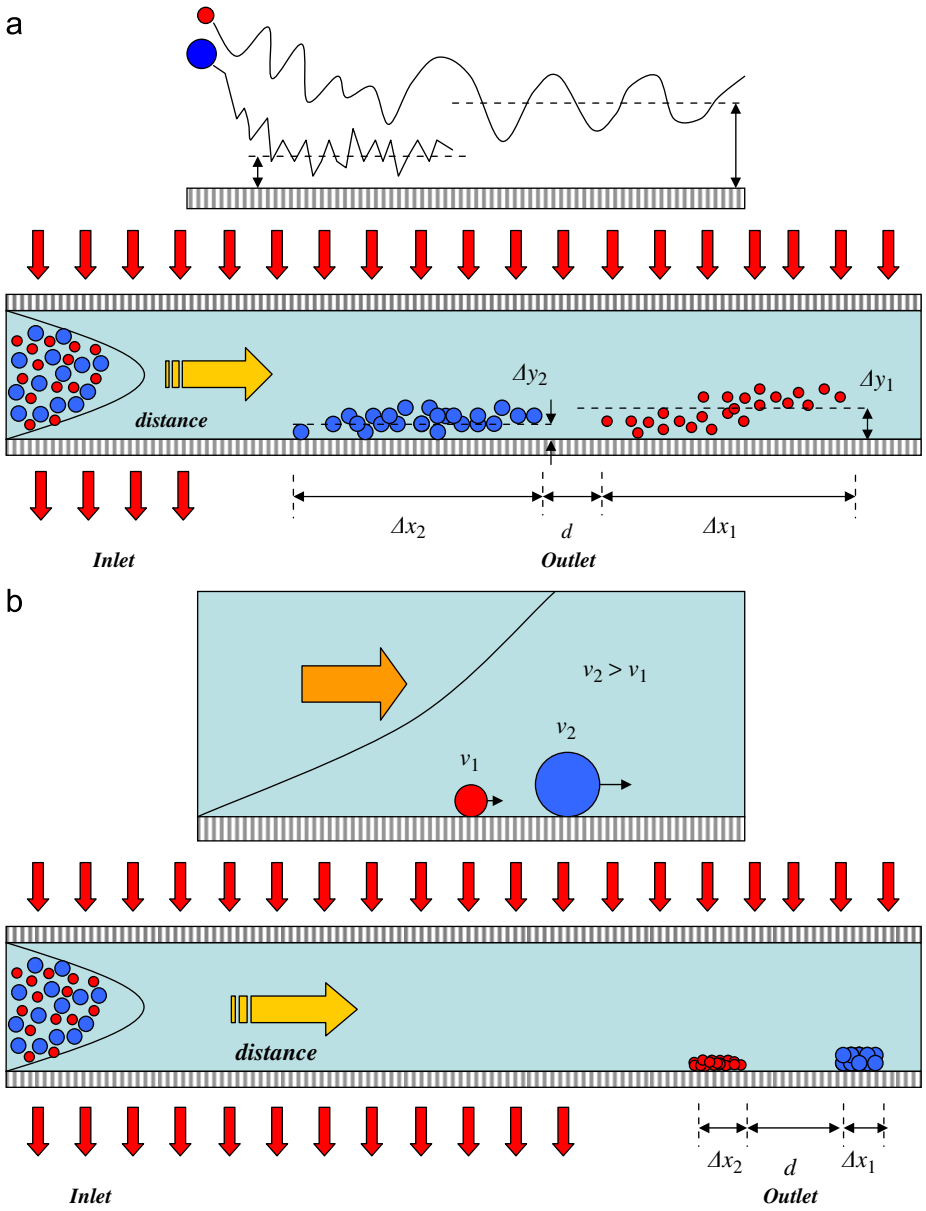

Fig. 2. (a) Normal mode separation in flow-FFF. (b) Steric mode separation in flow-FFF. In each case, the upper portion of the figure illustrates single particle behavior, and the lower portion illustrates the ensemble behavior.

A retention model which takes into account both normal mode diffusion and steric effects for spheres in RSF[4] was derived by Giddings (1978, 2000) and Giddings and Myers (1978)

$$R = 6(\alpha - \alpha^2) + 6\lambda(1 - 2\alpha)\left[\coth\left(\frac{1-2\alpha}{2\lambda}\right) - \frac{2\lambda}{1-2\alpha}\right] \tag{1.8}$$

where α is the ratio of the particle radius to gap thickness

$$\alpha = \frac{r}{H} \tag{1.9}$$

Eq. (1.8) reduces to Eq. (1.5) at small values of α. A comparison of the elution time behavior predicted by Eqs. (1.5) and (1.8) is shown in Fig. 3. The curve for normal mode elution shows a characteristic power law behavior on the log–log scale plot. However, the curve for Eq. (1.8) shows a distinct maximum in the elution time which occurs as approximately $\ell/r = 1$ (Phelan and Bauer, 2009). The maximum is called the steric transition and represents the point where large particles begin to elute more quickly than smaller ones. In general, the steric transition point shifts downward (to smaller particle size) with increasing cross flow rate. It is instructive to look at the asymptotic behavior for $\alpha \gg \lambda$. Under these conditions, Eq. (1.8) has the limiting value

$$\lim_{\alpha \gg \lambda} R = 6\alpha \cdot (1 - \alpha) \tag{1.10}$$

and thus, depends only on the size of the particles. The absence of diffusion in Eq. (1.10) indicates that the physics of the separation under steric conditions is controlled by a completely different mechanism than normal mode separation, and that the specific shape of the particle becomes important.

Measurements obtained for spheres often serve as a basis for calibrating the device for separations of more complex materials such as nanotubes under the assumption that particles of equal diffusivities elute at the same rate. However, the steric transition

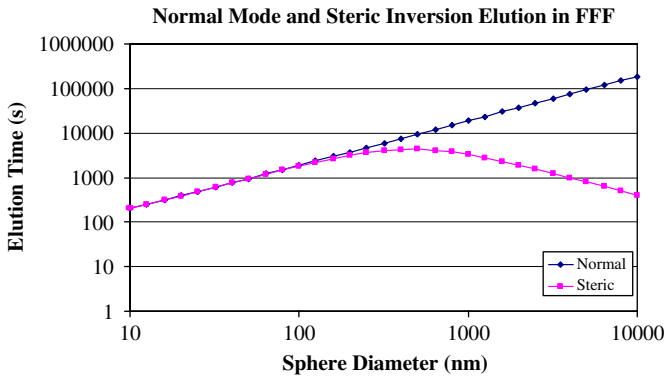

Fig. 3. Comparison normal mode and steric inversion elution time behavior in flow-FFF. The steric transition point shifts towards smaller particle size with increasing flow rate.

observed in flow-FFF with spheres is dictated by the interaction of the particle with the boundary, and thus, particle shape is bound to sharply influence the nature of this interaction. This means that under some conditions spheres and nanotubes of equivalent diffusivity may not elute at the same rate, and in this case calibration between the two based on this criterion would give erroneous results. This is bound to have important implications for understanding the separations of these materials, and we explore this here through the use of a simulation developed for flow-FFF. Nanotubes are of particular importance in the present study as we are investigating the length separation of singe wall carbon nanotubes (SWNTs) in flow-FFF experimentally (Chun et al., 2008), and understanding the elution mechanism is critical for interpreting the results.

In what follows, modeling of particle separation for spheres and rods of equal diffusivity is compared under conditions in which the sphere size spans the steric transition. The goal of this is to determine if, and under what conditions, the differences in particle shape becomes a significant factor in the elution behavior of the two different particle types, and to gain an understanding of the behavior of rods under conditions where the particles are highly retained. The paper is organized as follows. In the modeling section, we review the equations for the advection of spheres and rods in viscous flow with Brownian motion (Satoh, 2003; Kim and Karrila, 1991) and present a Brownian dynamics formulation for flow-FFF based on dilute solution behavior. The specific equation sets used to model flow-FFF based on the kinematics of RSF[4] are derived, along with a description of the numerical procedures and boundary conditions. For both cases, steric effects are accounted for by boundary conditions governing the point of closest approach. In the results section, calculations are shown first for the elution of spheres with sizes ranges spanning the steric transition. The results show that the model predicts a steric transition, and the results are in excellent agreement with the steric inversion theory of Giddings (Eq. (1.8)). The sphere calculations are then compared with rods of equal diffusivity under the same flow conditions. It is shown that at larger sizes, the rods begin to deviate from normal mode theory, but in the opposite sense as for spheres. In the Discussion, we examine the reasons for the divergence in behavior, and the implications in regard to calibrating FFF separations of nanotubes.

2. Modeling

2.1. Advection equations for spheres and rods

The simulation model for spheres used in this work is identical to that used in an earlier work (Phelan and Bauer, 2009), and is formulated under the assumption that the separations are carried out

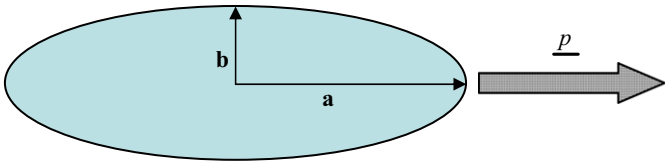

Fig. 4. Model parameters and orientation vector for the prolate ellipsoids particle model.

with dilute, aqueous solutions. Newtonian kinematics are used for the flow field, and the stresslet, hydrodynamic interactions (interparticle and particle-wall) and excluded volume are ignored. The dominant forces are the drag force due to fluid flow and Brownian motion. Lift forces (Williams et al., 1994) and buoyancy are also assumed to be negligible. Under these conditions, the linear momentum balance for an ensemble of spheres in a viscous flow, individually denoted by the superscript (i), is given by the Langevin equation (Satoh, 2003; Kim and Karrila, 1991),

$$\frac{d\underline{R}^{(i)}}{dt} = \underline{v}(\underline{R}^{(i)}) + \frac{\underline{F}_B^{(i)}(t)}{\zeta^{(i)}} \tag{2.1}$$

where $\underline{R}$ is the position vector of the particle, $\underline{v}(\underline{R})$ is the unperturbed velocity of the fluid evaluated at the particle position, $\underline{F}_B$ is the random force due to Brownian motion, and ζ is the Stokes' law drag coefficient given by

$$\zeta = 6\pi r\eta \tag{2.2}$$

where r is the particle radius, and η is the fluid viscosity. Details of the calculation of the Brownian force are described in Appendix A and Phelan and Bauer (2009).

The simulation model for rod-like particles used here is identical to that used in an earlier work (Phelan and Bauer, 2007) except for a slight modification of the boundary conditions, and the model is formulated using the same dilute solution assumptions as used for spheres. The nanotubes are modeled as prolate ellipsoids (Satoh, 2003; Kim and Karrila, 1991), shown in Fig. 4, which are formed by the rotation of an ellipse about its major axis. The object has a major axis of length, $2a$, a minor axis of length, $2b$, and is symmetric to the minor axis in the third direction. The orientation vector $\underline{p}$ describes the orientation of the major axis in 3-D space. The orientation vectors for the two perpendicular minor axes, $\underline{p}_{\perp 1}$ and $\underline{p}_{\perp 2}$, can be described in terms of $\underline{p}$ and are given in Appendix B.

The equations for the motion of an ellipsoid in a viscous fluid can be described as a stochastic form of the linear momentum balance with orientation dependent drag and diffusion coefficients, and a stochastic form of the Jeffery equation with orientation dependent rotational diffusion (Satoh, 2003; Kim and Karrila, 1991). The governing equations for an ensemble of ellipsoids, individually denoted by the superscript (i), are written as (Phelan and Bauer, 2007)

$$\frac{d\underline{R}^{(i)}}{dt} = \underline{v}(\underline{R}^{(i)}) + [\underline{\underline{\zeta}}^{(i)}]^{-1} \cdot \underline{F}_B^{(i)} \tag{2.3}$$

$$\frac{d}{dt}(\underline{p}^{(i)}) = -\underline{\underline{W}} \cdot \underline{p}^{(i)} + \lambda_p^{(i)}(\underline{\underline{D}} \cdot \underline{p}^{(i)} - \underline{\underline{D}} : \underline{p}^{(i)}\underline{p}^{(i)}\underline{p}^{(i)}) + \underline{p}^{(i)} \times [\underline{\underline{\xi}}^{(i)}]^{-1} \cdot \underline{T}_B^{(i)} \tag{2.4}$$

where $\underline{F}_B^{(i)}$ and $\underline{T}_B^{(i)}$ are the Brownian force and torque, respectively, $\underline{\underline{\zeta}}^{(i)}$ and $\underline{\underline{\xi}}^{(i)}$ are hydrodynamic resistance matrices given by

$$\underline{\underline{\zeta}}^{(i)} = \eta\{(X_A^{(i)} - Y_A^{(i)})\underline{p}^{(i)}\underline{p}^{(i)} + Y_A^{(i)}\underline{\underline{I}}\} \tag{2.5}$$

$$\underline{\underline{\xi}}^{(i)} = \eta\{(X_C^{(i)} - Y_C^{(i)})\underline{p}^{(i)}\underline{p}^{(i)} + Y_C^{(i)}\underline{\underline{I}}\} \tag{2.6}$$

$\underline{\underline{D}}$ and $\underline{\underline{W}}$ are the stretching and vorticity tensors, respectively,

$$\underline{\underline{D}} = \tfrac{1}{2}(\nabla \underline{v} + \nabla \underline{v}^T) \tag{2.7}$$

$$\underline{\underline{W}} = \tfrac{1}{2}(\nabla \underline{v} - \nabla \underline{v}^T) \tag{2.8}$$

and the quantity λ_p is a function of the particle aspect ratio, $\Re = \frac{a}{b}$, according to

$$\lambda_p = \frac{\Re^2 - 1}{\Re^2 + 1} \tag{2.9}$$

Relations for the quantities $X_A^{(i)}$, $Y_A^{(i)}$, $X_C^{(i)}$, and $Y_C^{(i)}$ are described in Appendix B. Details of the calculation of the Brownian force and torque are described in Appendix B and Phelan and Bauer (2007).

2.2. Model equations for RSF[4]

The geometry and processing parameters describing rectangular frit inlet symmetrical FFF (RSF[4]) are shown in Fig. 1. The channel has a throughput length L, a cross-flow direction thickness H, and a thickness in the third direction W. The flow rate in the throughput direction is Q_x, and is independent of the flow rate in the cross-flow direction, Q_y. The fluid velocity vector has two non-zero components, $\underline{v} = [v_x, v_y, 0]$. The velocity field in the throughput direction, v_x, is assumed to be parabolic, and the cross-flow velocity, v_y, is uniform. These velocity components are given by

$$v_x = 6u_{avg}\frac{y}{H}\left(1 - \frac{y}{H}\right) \tag{2.10}$$

$$v_y = -|v_{c,0}| \tag{2.11}$$

where u_{avg} and $|v_{c,0}|$ are average velocities given by

$$u_{avg} = \frac{Q_x}{HW} \tag{2.12}$$

$$|v_{c,0}| = \frac{Q_y}{LW} \tag{2.13}$$

For these kinematics, the equations governing the motion of the spheres are given by (Phelan and Bauer, 2009)

$$\frac{dR_x^{(i)}}{dt} = v_x(\underline{R}^{(i)}) + \frac{F_{B,x}^{(i)}}{\zeta^{(i)}} \tag{2.14}$$

$$\frac{dR_y^{(i)}}{dt} = v_y(\underline{R}^{(i)}) + \frac{F_{B,y}^{(i)}}{\zeta^{(i)}} \tag{2.15}$$

where v_x and v_y are given by Eqs. (2.10) and (2.11), respectively. Likewise, the governing equations for rods are given by (Phelan and Bauer, 2007)

$$\frac{dR_x^{(i)}}{dt} = v_x(\underline{R}^{(i)}) + v_{B,x}^{(i)} \tag{2.16}$$

$$\frac{dR_y^{(i)}}{dt} = v_y(\underline{R}^{(i)}) + v_{B,y}^{(i)} \tag{2.17}$$

$$\frac{d}{dt}(p_x^{(i)}) = \frac{1}{2}\frac{\partial v_x}{\partial y}p_y^{(i)}\left[1 + \lambda_p^{(i)}(1 - 2p_x^{(i)}p_x^{(i)})\right] + \dot{p}_{B,x}^{(i)} \tag{2.18}$$

$$\frac{d}{dt}(p_y^{(i)}) = \frac{1}{2}\frac{\partial v_x}{\partial y}p_x^{(i)}\left[-1 + \lambda_p^{(i)}(1 - 2p_y^{(i)}p_y^{(i)})\right] + \dot{p}_{B,y}^{(i)} \tag{2.19}$$

$$\frac{d}{dt}(p_z^{(i)}) = -\lambda_p^{(i)}p_x^{(i)}p_y^{(i)}p_z^{(i)}\frac{\partial v_x}{\partial y} + \dot{p}_{B,z}^{(i)} \tag{2.20}$$

where the velocity gradient is given by

$$\frac{\partial v_x}{\partial y} = \frac{6u_{avg}}{H}\left(1 - \frac{2y}{H}\right) \tag{2.21}$$

and $\underline{v}_B$ and $\underline{\dot{p}}_B$ are the effective translational velocity and rate of orientation change due to Brownian motion, whose components are given in Appendix B. These equations are integrated forward in time for each particle in the ensemble based on the initial conditions for particle position using a first order Euler integration scheme. The code is written in MATLAB.[1]

2.3. Boundary conditions

An important part of the scheme is the interaction of the particles with the boundaries. The cross flow velocity continually drives the particles towards the accumulation wall and the diffusion step being random may also cause the particles to collide with or overstep this boundary. To handle this, a no penetration boundary condition is used. This is implemented in a two step integration process, where first the advection step is carried out, the particles are checked for collision with the upper and lower surfaces in the thickness direction, and then the diffusion step is carried out, after which the particles are again checked for collision. In practice, the results are independent of whether the advection or diffusion is carried out first in the two-step scheme. However, it was found that a simple one step scheme where both advection and diffusion are combined gives deleterious results that agree with neither theory nor experiment (Phelan and Bauer, 2009). Since the length scale in the third direction in flow-FFF is generally around 100 times larger than the cross flow direction and there is no flow component in this direction, interaction of particles with these walls is ignored.

For spheres, particles may only approach within a distance equal to one particle radius of the upper and lower boundaries, as shown in Fig. 5a. If it is determined that particles have advected or diffused within one radius of a surface their positions are reset to the point at which they collided. At subsequent time steps, such particles are then allowed to undergo diffusion away from the surface, and x-component of the velocity is given by $v_x = v_x(r_i)$, where r_i is the particle radius. A similar scheme is used for ellipsoids as shown in Fig. 5b. In this case, the particles may only approach within a distance $\delta = a|\sin\theta\cos\phi|$, where (θ, ϕ) is the angular position of the rod in spherical coordinates with respect to the center of mass of the object. The orientation has a relationship with the spherical coordinate system given by (Zhang et al., 2005)

$$\underline{p} = [\cos\theta, \sin\theta\cos\phi, \sin\theta\sin\phi] \tag{2.22}$$

Thus, $\delta = a|p_y|$, and the boundary condition for the velocity is $v_x = v_x(\delta_i)$.

3. Results

3.1. Calculation of equivalent diffusion

In terms of application to FFF, there are two choices for the diffusion coefficient which governs the retention for ellipsoids. The Perrin (1936) diffusivity applies to the case in which particles are randomly oriented

$$D = \left(\frac{kT}{6\pi\eta a}\right)\frac{1}{s}\ln\left[\frac{1+s}{\Re}\right] \tag{3.1}$$

[1] Identification of a commercial product is made only to facilitate reproducibility and to adequately describe procedure. In no case does it imply endorsement by the National Institute of Standards and Technology (NIST) or imply that it is necessarily the best product for the procedure.

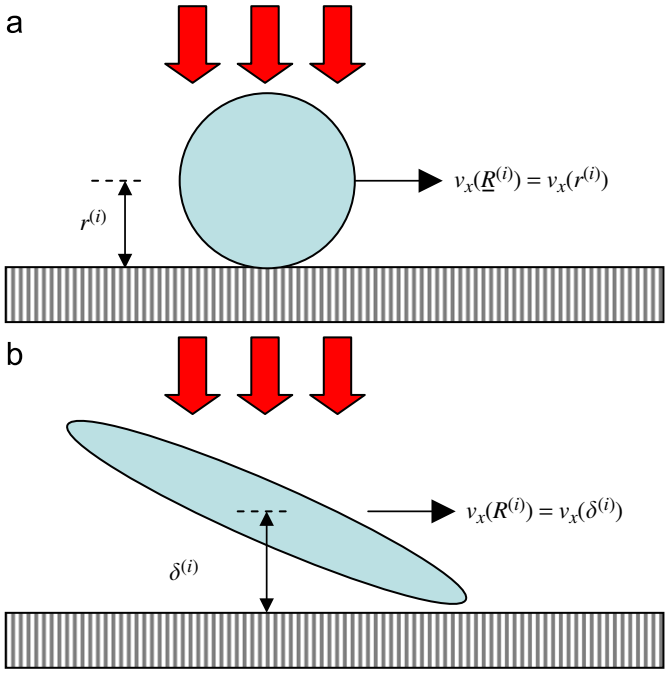

Fig. 5. Size exclusion boundary conditions used in the flow simulation: (a) spherical particles and (b) ellipsoidal particles.

where $s=\sqrt{1-\Re^2}$. The other choice is the transverse diffusion coefficient of the model, $D_{T,\perp}=kT/\eta Y_A$ (see Appendix B). We show below that the transverse coefficient best describes the elution behavior for ellipsoids under conditions of low retention as the particles spend the majority of the time oriented in the flow direction. If one equates this value with the sphere diffusivity, i.e., $D_{eq}=kT/\zeta=kT/\eta Y_A$, one can solve for the radius of the sphere of equivalent diffusivity in terms of the ellipsoid size

$$r_{eq}=a\frac{16}{3}\frac{s^3}{2s+(3s^2-1)Z} \tag{3.2}$$

where Z is a function of s given in Appendix B. Using Eq. (3.2), a table of equivalent sphere and ellipsoid sizes for an ellipsoid diameter of 1 nm (i.e., $b=0.5$) is constructed and shown in Table 1.

3.2. Characteristic dispersion and elution

The simulation procedure and characteristic output are illustrated using results for the elution of 49.64 nm (i.e., approximately 50 nm) spheres and 250 nm ellipsoids (case 9 in Table 1). The processing parameters given in Table 2 are used throughout. For these size particles under these conditions, the normal mode retention has a value of $R=0.051$. An ensemble size of 1000 particles was used in all the calculations. Previous study has shown that the mean elution time is relatively insensitive to ensemble size, and that an ensemble of this size gives smooth elution profiles (Phelan and Bauer, 2007, 2009).

The first step in the simulation is to emulate the experimental focusing step which concentrates the species at a particular point in the flow device in order to obtain a more uniform elution profile. The initial condition that results from this is illustrated in Fig. 6a for the case of the 50 nm spheres (the vertical axis has been greatly dilated for clarity). In the focusing step, the output flow in the throughput direction is reversed and balanced with the horizontal input flow forcing all the particles to a common horizontal staring point in the apparatus, x_f, called the focus point. In the vertical direction, the particles discretely follow the normalized equilibrium profile given by Eq. (1.3), using the focusing flow rate (Table 1) to calculate the distribution. The discrete distribution for 1000 particles is shown in Fig. 6b (note that the x-axis of the plot only extends 1/10 if the way through the gap). Since the distribution is exponential, the particle concentration greatly increases as the profile nears the wall.

Fig. 6c shows the distribution of the spheres in the device under throughput conditions when the particles have advanced approximately half-way down the channel. It can be seen from the figure that once the flow starts, there is a great amount of dispersion in the throughput direction. This effect is due to both the non-homogeneous initial condition in the y-direction, and the random nature of the particle diffusion. A close-up of the particle cloud is shown in the inset to Fig. 6c and indicates that while the particles travel very close to the wall, very few of them touch the wall at a given instant. Because of the dispersion, even for monodisperse systems there is a distribution of residence times.

A comparison of the elution profiles for the 50 nm spheres and 250 nm rods is shown in Fig. 7. Under these conditions, the distributions are similar but not identical. The average particle residence time for the spheres is 980.1 ± 46.1s, and the distribution exhibits a slightly negative skewness of -0.2 and positive kurtosis of 0.46. For the rods, the average particle residence time is 989.9 ± 46.1s, and the distribution also exhibits a slightly negative skewness of -0.13 but a negligible kurtosis of 0.01. For both systems, the

Table 1
Table of equivalent diffusivity sizes for ellipsoids and spheres, based on the transverse diffusivity of the ellipsoids.

Equivalent diffusion for ellipsoids and spheres		
Ellipsoid length (nm)	Sphere diameter (nm)	D (m^2/s)
40	10.92	3.93×10^{-11}
50	13.06	3.29×10^{-11}
64	15.94	2.69×10^{-11}
80	19.13	2.24×10^{-11}
100	23.00	1.87×10^{-11}
128	28.23	1.52×10^{-11}
160	34.03	1.26×10^{-11}
200	41.08	1.04×10^{-11}
250	49.64	8.65×10^{-12}
320	61.29	7.00×10^{-12}
400	74.23	5.78×10^{-12}
500	90.00	4.77×10^{-12}
640	111.48	3.85×10^{-12}
800	135.40	3.17×10^{-12}
1000	164.59	2.61×10^{-12}
1280	204.45	2.10×10^{-12}
1600	248.90	1.72×10^{-12}
2000	303.24	1.42×10^{-12}
2500	369.66	1.16×10^{-12}
3200	460.56	9.32×10^{-13}
4000	562.16	7.64×10^{-13}
5000	686.55	6.25×10^{-13}
6400	857.00	5.01×10^{-13}
8000	1047.77	4.10×10^{-13}

Table 2
Processing parameters used in the simulations.

Processing parameters	
Length, L (m)	0.25
Thickness, H (m)	0.00025
Width, W (m)	0.02
Focus point, x_f (m)	0.01
T (K)	293
Viscosity (Pa s)	0.001
Q_x (m^3/s)	2.5×10^{-8}
Q_y (m^3/s)	2.0×10^{-8}
Q_f (m^3/s)	2.0×10^{-8}

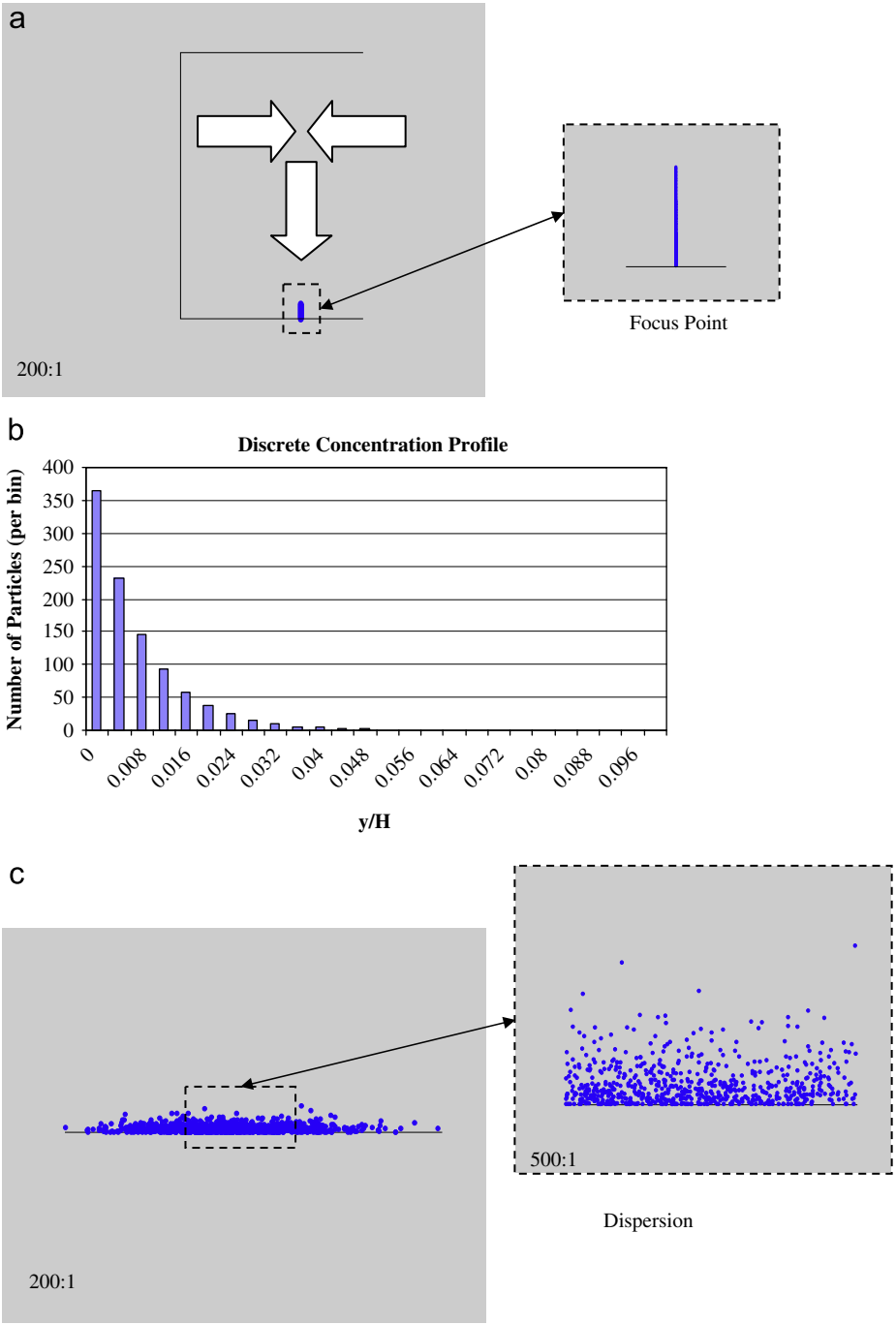

Fig. 6. (a) Initial condition used for a simulation of 50 nm spheres, with a focusing flow rate of 2.0×10^{-8} m^3/s, for an ensemble of 1000 particles, (b) discrete concentration profile for the initial condition of the 50 nm spheres, and (c) illustration of particle dispersion for 50 nm spheres approximately mid way through the elution. The inset illustrates the fine details of the particle cloud.

particles exit in approximately ± 3 standard deviations about the mean. The mean and standard deviations for the two systems are essentially identical, but the fatter front end tail of the spheres is evident. The only other significant difference between the two particle types under these normal mode conditions is the kurtosis indicating that the rods are closer to being normally distributed than the spheres.

3.3. Calculations for equivalent diffusion

The simulation was used to model the elution of spheres and ellipsoids for the particle sizes shown in Table 1. Fig. 8 compares the mean elution time for spheres calculated from the simulation with both normal mode theory and the steric inversion theory of Giddings (Eq. (1.8)). Steric inversion is evident in the simulation results and under these conditions, the steric transition occurs at a particle size of 460 nm. The simulation begins to strongly deviate from normal mode theory at a sphere size of about 200 nm. However, the agreement between the simulation and the steric theory is very good across the entire range of particle sizes. On average, the simulation times are within 5% of the steric theory, with the maximum deviation being about 7.5% higher close to the steric transition point. This is a good indicator that the boundary condition used captures the most of the essential physics.

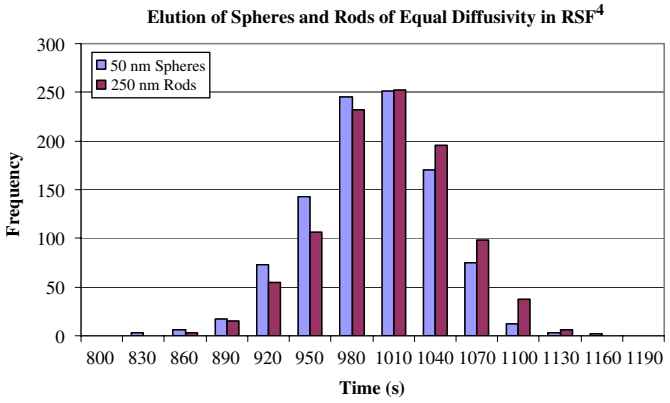

Fig. 7. Comparison of the elution behavior for 50 nm spheres and 250 nm ellipsoids. The particles have equivalent diffusivity based on the transverse diffusion coefficient of the model.

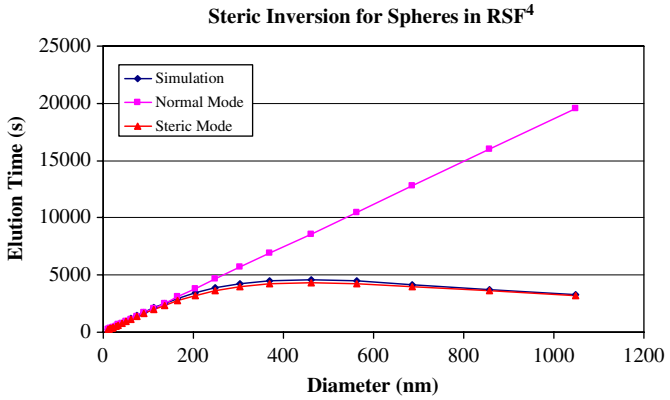

Fig. 8. A comparison of simulation predictions for mean elution time of spheres in RSF4 with normal mode and steric inversion theory.

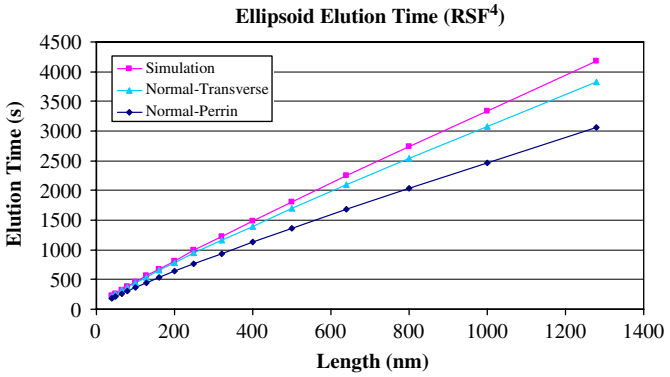

Fig. 9. A comparison of simulation predictions for ellipsoids in RSF4 with normal mode theory using both the transverse and Perrin diffusivity values to calculate the retention.

Fig. 9 shows the mean elution time calculated from the simulation for ellipsoids vs. length and it is evident from the data that steric inversion does not take place for rod-like particles as it does for spheres. In the figure, the simulation data is compared with normal mode theory using both the transverse and Perrin diffusivity values to calculate the retention. Under these highly retained conditions, the curve for the transverse coefficient more closely matches the simulation values. Agreement between the simulation and the transverse normal mode curve is extremely good up to about 300 nm, but from that point there is a slow divergence, with the simulation values becoming increasingly longer.

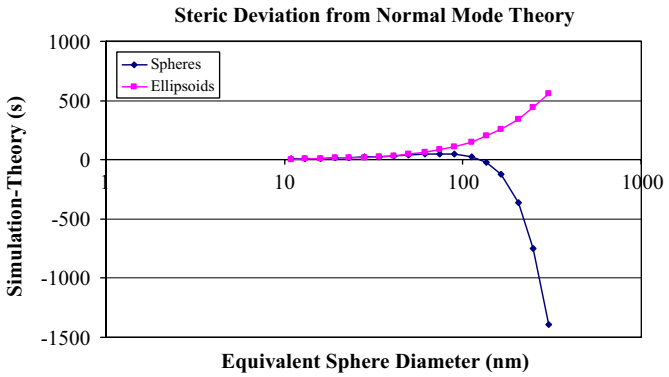

Fig. 10. A comparison of steric deviation from normal mode theory for spheres and ellipsoids plotted as a function of equivalent sphere size.

A comparison of the relative steric effects for the two particle types is shown in Fig. 10, which plots the deviations from normal mode theory for spheres and rods vs. the equivalent sphere diameter. From a calibration standpoint, differences between the two become appreciable at a sphere size of approximately 100 nm which corresponds to a rod size on the order of 500 nm. While this is technically below the steric transition point for spheres, it shows that steric effects begin to affect the results long before the actual inversion takes place. The relative contributions of each to the total difference in elution time is relative equal until a sphere size of about 160 nm (rod size = 1000 nm). However, as this point the deviations for spheres become sharper and more drastic than they are for rods.

4. Discussion

The primary objective of this work was to compare simulations for particle elution in FFF for different particle types. The simulations were performed using a Brownian dynamics simulation which takes into account the drag force due to fluid flow, and the diffusion of the particles due to Brownian motion, which are the dominant forces under dilute solution conditions. The boundary conditions also play an important role in the results, as will be discussed. The goal here was two-fold. First, it was of interest to determine whether or not spheres and rods of equal diffusivity elute at the same rate, and if not, to find at what point the two systems show a divergence in behavior. This is important because monodisperse spheres are used to calibrate measurements of more complex materials in FFF, and equivalent diffusion is used as the calibration measure. Second, it was largely an unknown as to whether or not rod-like particles would exhibit a similar steric inversion type phenomenon that spheres exhibit in flow-FFF. This would potentially limit the utility of FFF as a length sorting device for long nanotubes.

The first item studied was the elution of spheres with a size range from approximately 10 to 1000 nm, which is broad enough to span the steric transition. The simulation predictions for mean elution time are in excellent agreement with the steric inversion theory of (Giddings, 1978, 2000), showing an average 5% deviation across the entire spectrum of particle sizes. This is a fairly stringent test for the simulation as the elution behavior transitions from completely normal mode separation at the low end of the particle size spectrum to completely steric mode separation at the other. This gives us good confidence that the appropriate physics is being captured, particularly in regard to the boundary conditions. In addition, we note that the simulation qualitatively captures the experimental observation

that the elution distribution for spheres becomes increasingly narrow as one advances higher into the steric mode region.

The first comparison between different particle types were the elution fractograms for (the approximately) 50 nm spheres and 250 nm ellipsoids, which have equivalent diffusivity based on the transverse diffusion coefficient of the ellipsoid. The results show that under normal mode conditions, the elution distributions of the two systems are essentially identical, as is expected by theory. The only significant difference between the distributions was that the kurtosis for the rod-like particles indicates that they are closer to being normally distributed than the spheres, and the sphere distribution has a manifestly larger front end tail than the rods. As the mean residence time for the spheres is slightly shorter than for the rods, this may be an early but weak manifestation of the different size exclusion properties of the particles at the boundary which causes the spheres to speed up, and the rods to align. However, calculations in the normal mode region reasonably met expectations.

The simulations results for ellipsoids show a number of things that were of importance to us. First, for rod-like particles steric inversion akin to that observed for spheres of equal diffusivity is not observed. Rather, the rods continue to elute by a normal mode mechanism up to a size of approximately 500 nm (based on our assumption of a 1 nm diameter), and up to this point the retention behavior is well described by the transverse diffusion coefficient of the model. Past this point, the rods begin to elute increasingly slower than predicted by normal mode theory. This trend continues up to the maximum rod length simulated, 2000 nm, with no sign of inversion. Based on the underlying physics, it seems quite plausible to speculate that this inverse steric effect occurs for rods due to alignment of the rods in the low velocity region along the accumulation wall (whereas the spheres are sterically hindered from approaching the wall). The reasoning for this is that as the particle size gets larger, the rods rotate with decreased frequency due to shear and they also become less diffusive, both translationally and rotationally. The decrease in both modes of rotation allows the particles to more closely approach the wall (based on the steric exclusion boundary condition), and the decrease in translational diffusion limits their movement away from the wall. Thus, as diffusion becomes less dominant in flow-FFF, the elution behavior is strongly dictated by the shape of the particle, the behavior of the particle in the flow field, and the interaction between the particle and the boundary.

This finding has practical implications experimentally in regard to the separation of nanotubes. First, the lack of steric inversion for rod-like particles is in some ways a positive result as these systems will not have overlapping size fractions, but can continue to be size sorted with increasing length (of course, the required elution time will also increase, but that is another matter). In addition, the different modes of separation can potentially be used advantageously to eliminate spherical impurities of equivalent diffusivity in systems of longer rods, something which is much harder to do for shorter rods. On the other hand, the results show that the calibration of such systems with spheres of equivalent diffusivity can become flawed at large sizes. At a certain point, the negative deviations from normal mode behavior for the spheres and the positive deviations for the rods lead to increasingly greater differences in mean elution times. While the steric effect is not so sharp for rods as it is for spheres, the divergent behavior means that the total difference between the two can become quite considerable, as evidenced by the results in Fig. 10. Of course, the exact size at which calibration breaks down depends on experimental conditions, and the effect can be lessened by shifting the steric inversion point for the spheres to larger sizes. This may, however, limit operating conditions.

Another finding that comes out this study is that for small to medium sized rods, the elution behavior correlates with transverse diffusion coefficient of the ellipsoidal model, rather than the Perrin diffusivity (orientation averaged behavior), whereas, in an earlier study we showed that the retention correlated with the Perrin diffusivity (Phelan and Bauer, 2007). The difference can be attributed to the relative value of the retention in the two studies. In the present case, the retention values for the ellipsoidal particles were all in the range $R \leqslant 0.1$. In the former case, the retention values were in the range $R \geqslant 0.2$. This indicates that there is a transition in the dominant mode of transverse diffusion behavior as the retention becomes smaller, with alignment in the flow direction playing an increasingly important role. This transition is consistent with the steric slow down that is eventually observed at large rod sizes.

The particular results shown here are for the FFF variant dubbed as RSF[4]—the simulation is also programmed to simulate the processing variant known frit-inlet asymmetrical field-flow fractionation (FIA-FFF) for both rectangular and trapezoidal cross-sections. However, it is not expected that such processing variations would have any effect on the conclusions reached here. An additional factor is that we only looked at ellipsoids of 1 nm diameter, and tube size can run from 1 to 4 nm. However, this also probably does not have too large an effect on the length interpretation reached here as rods of 4 nm diameter have a length that is only about 20–25% shorter than rods of equivalent diffusivity with 1 nm diameter.

A number of items might be pursued in future work. The boundary conditions used in the simulation for both spheres and ellipsoids undoubtedly play a very important role in the results obtained here. The different behavior of the particle types in the steric region is dictated by interaction of the particles at the boundary. At larger sizes, spheres speed up due to size exclusion, while rods slow down due to increasing alignment. The boundary conditions used for both particle types are undoubtedly a simplification of the detailed physics. For spheres, it is likely that the small amount of diffusivity possessed by the larger particles and possibly even some very small lift forces (which Giddings and others—Williams et al., 1992, 1994, 199a,b, 1997, 2001; Giddings et al., 1991; Zhang et al., 1994; Jensen et al., 1996; Jiang et al., 1999—have shown can have an effect for larger particles in FFF) act to eliminate friction with surface, and that the velocity boundary condition is very appropriate. Based on the agreement between the simulation and the steric inversion theory, this would seem to be the case.

However, for the rod-like particles, the situation is more complex and there is some additional physics we may want to consider to gain a greater understanding of the steric effect. The boundary condition used here hinders the translation movement of the particles near the wall, but not the rotational movement. The importance of this is that once the rotational movement is hindered, the cross flow then creates a torque on the particles that will act to further align the particles with the wall, and this torque is not presently modeled. Thus, the present approximation represents a minimal alignment condition and it is likely that the actual effect is stronger. It may be of interest to incorporate this additional physics. On the experimental side, it is desirable to test the flow code for rod-like particles against experimental data. This is made somewhat difficult by the fact that it is difficult to obtain monodisperse solutions of rod-like particles akin to nanotubes, so simulations must be compared with fractions which have a distribution of sizes. On-line size sensitive detection such as multi angle light scattering can been used to measure rod lengths as a function of elution times. Also, it may be possible to collect fractions at different elution times and measure their lengths by microscopy. Such measurements are underway in our laboratory.

Another interesting possibility that the calculations point to is using steric effects to create a new mode of separation of rod-like particles in flow-FFF by aligning the particles in the field direction, transverse to the flow, for example, with a dielectric field. The calculations for the sterically hindered spheres indicate that this induces a great speed up in the elution, and the same would be even truer for rods due to their great length. This would be beneficial in two ways. First, the elution of very long rods which are slow in normal

mode elution, would be greatly accelerated. In addition, if nanotubes of different type (i.e., semi-conductors and metallics) could be preferentially aligned, it would provide a very nice means for producing chiral based separations in flow-FFF.

5. Summary and conclusions

The elution of spheres and rods of equal diffusivity in FFF was studied using a Brownian dynamics method. Results for spheres show that the simulation correctly models the steric transition, and the mean elution time behavior is well described by the steric inversion theory of Giddings (1978, 2000) and Giddings and Myers (1978). The results for rods show that nanotube size particles elute by a normal mode mechanism up to a length of approximately 500 nm (based on a particle diameter of 1 nm). At larger sizes, an inverse steric effect is observed in which larger rods move increasingly slower than predicted by theory (in the present case up to lengths of 2000 nm, with no sign of inversion). The different behavior of the particle types is dictated by interaction of the particles at the boundary. At larger sizes, spheres speed up due to size exclusion, while rods slow down due to increasing alignment. Spheres and rods of equivalent diffusivity elute at the same rate up to a sphere size of approximately 90 nm (500 nm rods), at which point there are increasingly greater differences in mean elution times. This affects the calibration of such operations, but also shows that length based separations for nanotubes are not bound by the same limitation as occurs for spheres due to steric inversion.

Appendix A. Properties of spheres

The linear momentum balance for the advection of a spherical particle in a viscous flow can be written as

$$m\frac{\mathrm{d}\underline{U}}{\mathrm{d}t} = -\underline{F}_D(t) + \underline{F}_B(t) \tag{A.1}$$

where $\underline{F}_D$ is the fluid–particle drag force, and $\underline{F}_B$ is the random force due to Brownian motion. For a spherical particle, the drag force is given by

$$\underline{F}_D(t) = \zeta(\underline{U} - \underline{v}) \tag{A.2}$$

where ζ is Stokes' law drag coefficient given by

$$\zeta = 6\pi r\eta \tag{A.3}$$

r is the radius of the particle, η is the viscosity of the fluid, $\underline{U}$ is the velocity of the particle, and $\underline{v}$ is the unperturbed velocity of the fluid evaluated at the particle position. Under the assumption of negligible inertia, i.e., $m(\mathrm{d}\underline{U}/\mathrm{d}t) \approx 0$, Eq. (A.1) can be written as

$$\frac{\mathrm{d}\underline{R}}{\mathrm{d}t} = \underline{v}(\underline{R}) + \frac{\underline{F}_B(t)}{\zeta} \tag{A.4}$$

where $\underline{R}$ is the position vector of the particle.

In order for the dynamics in the computation of the random Brownian force to satisfy the fluctuation–dissipation theorem, the values for the Brownian force must satisfy the relationships

$$\langle \underline{F}_B^{(i)}(t)\rangle = 0 \tag{A.5}$$

$$\langle \underline{F}_B^{(i)}(t)\underline{F}_B^{(j)}(t')\rangle = 2kT\zeta\delta_{ij}\delta(t-t')\,\underline{\underline{I}} \tag{A.6}$$

where k is Boltzmann's coefficient, T is the absolute temperature, δ_{ij} is the Kronecker delta, $\delta(t-t')$ is the dirac delta function, and the operator $\langle\cdots\rangle$ indicates an average over the ensemble of the random force.

For spheres, the Brownian force has magnitude

$$F_B^{(i)} = \zeta^{(i)}\sqrt{\frac{2\cdot d\cdot D^{(i)}}{\Delta t}} \tag{A.7}$$

and the components along a Cartesian axis are given by (Satoh, 2003)

$$F_{B,x}^{(i)} = \zeta^{(i)}\sqrt{\frac{2\cdot d\cdot D^{(i)}}{\Delta t}}\cdot r_x^{(i)} \tag{A.8}$$

$$F_{B,y}^{(i)} = \zeta^{(i)}\sqrt{\frac{2\cdot d\cdot D^{(i)}}{\Delta t}}\cdot r_y^{(i)} \tag{A.9}$$

$$F_{B,z}^{(i)} = \zeta^{(i)}\sqrt{\frac{2\cdot d\cdot D^{(i)}}{\Delta t}}\cdot r_z^{(i)} \tag{A.10}$$

where d is the dimension of the system (1-D, 2-D, or 3-D), Δt is the time step used in the simulation, $D^{(i)}$ is the Stokes–Einstein diffusion coefficient given by

$$D^{(i)} = \frac{kT}{\zeta^{(i)}} \tag{A.11}$$

and $[r_x^{(i)}, r_y^{(i)}, r_z^{(i)}]$ are a normalized set of random numbers.

Appendix B. Properties of prolate spheroids

B.1. Orientation

The orientation vectors of the two perpendicular minor axes, $\underline{p}_{\perp 1}$ and $\underline{p}_{\perp 2}$, can be described in terms of $\underline{p}$. First, the orientation vector $\underline{p} = [p_x, p_y, p_z]$ is renormalized such that

$$\underline{p}' = \frac{1}{\alpha}[p_x, p_y, p_z] \tag{B.1}$$

where $\alpha = \sqrt{p_x^2 + p_y^2 + p_z^2}$. The components of the orientation vectors $\underline{p}_{\perp 1}$ and $\underline{p}_{\perp 2}$ are given in terms of $\underline{p}$ and α by

$$\underline{p}_{\perp 1} = \left[\frac{-p_y}{\sqrt{p_x^2+p_y^2}}, \frac{p_x}{\sqrt{p_x^2+p_y^2}}, 0\right] \tag{B.2}$$

$$\underline{p}_{\perp 2} = \left[\frac{-p_x p_z}{\alpha\sqrt{p_x^2+p_y^2}}, \frac{-p_y p_z}{\alpha\sqrt{p_x^2+p_y^2}}, \frac{p_x^2+p_y^2}{\alpha\sqrt{p_x^2+p_y^2}}\right] \tag{B.3}$$

B.2. Resistance matrices

For prolate spheroids the translational resistance matrix $\underline{\underline{\zeta}}^{(i)}$ is described in terms of the orientation vector $\underline{p}^{(i)}$ by the relations

$$\underline{\underline{\zeta}}^{(i)} = \eta\{(X_A^{(i)} - Y_A^{(i)})\underline{p}^{(i)}\underline{p}^{(i)} + Y_A^{(i)}\underline{\underline{I}}\} \tag{B.4}$$

where

$$\frac{X_A}{6\pi a} = \frac{8}{3}\cdot\frac{s^3}{-2s + (1+s^2)\mathrm{Z}} \tag{B.5}$$

$$\frac{Y_A}{6\pi a} = \frac{16}{3}\cdot\frac{s^3}{2s + (3s^2-1)\mathrm{Z}} \tag{B.6}$$

s is the ellipsoid eccentricity given by

$$s = \frac{\sqrt{a^2-b^2}}{a} \tag{B.7}$$

and Z is given in terms of s by

$$Z = \ln \frac{(1+s)}{(1-s)} \tag{B.8}$$

The rotational resistance matrix $\underline{\underline{\xi}}^{(i)}$ is defined by the relations

$$\underline{\underline{\xi}}^{(i)} = \eta \left\{ (X_C^{(i)} - Y_C^{(i)}) \underline{p}^{(i)} \underline{p}^{(i)} + Y_C^{(i)} \underline{\underline{I}} \right\} \tag{B.9}$$

$$\frac{X_C}{8\pi a^3} = \frac{4}{3} \cdot \frac{s^3(1-s^2)}{2s-(1-s^2)Z} \tag{B.10}$$

$$\frac{Y_C}{8\pi a^3} = \frac{4}{3} \cdot \frac{s^3(2-s^2)}{-2s+(1+s^2)Z} \tag{B.11}$$

The resistance matrices have the analytical inverses

$$[\underline{\underline{\zeta}}^{(i)}]^{-1} = \frac{1}{\eta} \left\{ \left(\frac{1}{X_A^{(i)}} - \frac{1}{Y_A^{(i)}} \right) \underline{p}^{(i)} \underline{p}^{(i)} + \frac{1}{Y_A^{(i)}} \underline{\underline{I}} \right\} \tag{B.12}$$

$$[\underline{\underline{\xi}}^{(i)}]^{-1} = \frac{1}{\eta} \left\{ \left(\frac{1}{X_C^{(i)}} - \frac{1}{Y_C^{(i)}} \right) \underline{p}^{(i)} \underline{p}^{(i)} + \frac{1}{Y_C^{(i)}} \underline{\underline{I}} \right\} \tag{B.13}$$

B.3. Brownian force

In order for the dynamics to satisfy the fluctuation–dissipation theorem, the values for the Brownian forces and torques must satisfy the relationships (Cobb and Byron, 2005; Cobb and Butler, 2006)

$$\langle \underline{F}_B^{(i)}(t) \rangle = 0 \tag{B.14}$$

$$\langle \underline{T}_B^{(i)}(t) \rangle = 0 \tag{B.15}$$

$$\langle \underline{F}_B^{(i)}(t) \underline{F}_B^{(i)}(t') \rangle = 2kT \underline{\underline{\zeta}}^{(i)} \delta(t-t') \tag{B.16}$$

$$\left\langle \underline{T}_B^{(i)}(t) \underline{T}_B^{(i)}(t') \right\rangle = 2kT \underline{\underline{\xi}}^{(i)} \delta(t-t') \tag{B.17}$$

where k is Boltzmann's constant, T is the absolute temperature, δ_{ij} is the Kronecker delta, $\delta(t-t')$ is the dirac delta function, and the operator $\langle \ldots \rangle$ indicates an average over the ensemble of the random force.

The translational Brownian force term can be decomposed as (Satoh, 2003)

$$\left[\underline{\underline{\zeta}}^{(i)} \right]^{-1} \cdot \underline{F}_B^{(i)} = \frac{F_{B,\parallel}^{(i)}}{\zeta_\parallel^{(i)}} \underline{p}^{(i)} + \frac{F_{B,\perp 1}^{(i)}}{\zeta_{\perp 1}^{(i)}} \underline{p}_{\perp 1}^{(i)} + \frac{F_{B,\perp 2}^{(i)}}{\zeta_{\perp 2}^{(i)}} \underline{p}_{\perp 2}^{(i)} \tag{B.18}$$

where the forces $F_{B,\parallel}^{(i)}$, $F_{B,\perp 1}^{(i)}$ and $F_{B,\perp 2}^{(i)}$ are the Brownian forces and drag coefficients parallel and perpendicular to the orientation of the ellipsoids with magnitude

$$F_{B,||}^{(i)} = \zeta_{||}^{(i)} \sqrt{\frac{2 \cdot d \cdot D_{T,\parallel}^{(i)}}{\Delta t}} \cdot r_{||}^{(i)} \tag{B.19}$$

$$F_{B,\perp 1}^{(i)} = \zeta_{\perp 1}^{(i)} \sqrt{\frac{2 \cdot d \cdot D_{T,\perp 1}^{(i)}}{\Delta t}} \cdot r_{\perp 1}^{(i)} \tag{B.20}$$

$$F_{B,\perp 2}^{(i)} = \zeta_{\perp 2}^{(i)} \sqrt{\frac{2 \cdot d \cdot D_{T,\perp 2}^{(i)}}{\Delta t}} \cdot r_{\perp 2}^{(i)} \tag{B.21}$$

$[r_\parallel^{(i)}, r_{\perp 1}^{(i)}, r_{\perp 2}^{(i)}]$ are a normalized set of random numbers, the scalar d is the dimension of the system, and the translational drag and diffusion coefficients are given respectively by the relations

$$\zeta_\parallel^{(i)} = \eta X_A^{(i)} \tag{B.22}$$

$$\zeta_{\perp 1}^{(i)} = \zeta_{\perp 2}^{(i)} = \zeta_\perp^{(i)} = \eta Y_A^{(i)} \tag{B.23}$$

$$D_{T,\parallel}^{(i)} = \frac{kT}{\zeta_\parallel^{(i)}} \tag{B.24}$$

$$D_{T,\perp 1}^{(i)} = D_{T,\perp 2}^{(i)} = \frac{kT}{\zeta_\perp^{(i)}} \tag{B.25}$$

In a similar manner, the Brownian torque can be decomposed as

$$[\underline{\underline{\xi}}^{(i)}]^{-1} \cdot \underline{T}_B^{(i)}(t) = \frac{T_{B,\parallel}^{(i)}}{\xi_\parallel^{(i)}} \underline{p}^{(i)} + \frac{T_{B,\perp 1}^{(i)}}{\xi_{\perp 1}^{(i)}} \underline{p}_{\perp 1}^{(i)} + \frac{T_{B,\perp 2}^{(i)}}{\xi_{\perp 2}^{(i)}} \underline{p}_{\perp 2}^{(i)} \tag{B.26}$$

where the torques $T_{B,\parallel}^{(i)}$, $T_{B,\perp 1}^{(i)}$ and $T_{B,\perp 2}^{(i)}$ are the components parallel and perpendicular to the orientation of the ellipsoids with magnitude

$$T_{B,||}^{(i)} = \xi_{||}^{(i)} \sqrt{\frac{2 \cdot d \cdot D_{R,||}^{(i)}}{\Delta t}} \cdot r_{||}^{(i)} \tag{B.27}$$

$$T_{B,\perp 1}^{(i)} = \xi_{\perp 1}^{(i)} \sqrt{\frac{2 \cdot d \cdot D_{R,\perp 1}^{(i)}}{\Delta t}} \cdot r_{\perp 1}^{(i)} \tag{B.28}$$

$$T_{B,\perp 2}^{(i)} = \xi_{\perp 2}^{(i)} \sqrt{\frac{2 \cdot d \cdot D_{R,\perp 2}^{(i)}}{\Delta t}} \cdot r_{\perp 2}^{(i)} \tag{B.29}$$

$[r_\parallel^{(i)}, r_{\perp 1}^{(i)}, r_{\perp 2}^{(i)}]$ are a second normalized set of random numbers, and the rotational drag and diffusion coefficients are given by

$$\xi_\parallel^{(i)} = \eta X_C^{(i)} \tag{B.30}$$

$$\xi_{\perp 1}^{(i)} = \xi_{\perp 2}^{(i)} = \xi_\perp^{(i)} = \eta Y_C^{(i)} \tag{B.31}$$

$$D_{R,||}^{(i)} = \frac{kT}{\xi_{||}^{(i)}} \tag{B.32}$$

$$D_{R,\perp 1}^{(i)} = D_{R,\perp 2}^{(i)} = \frac{kT}{\xi_\perp^{(i)}} \tag{B.33}$$

Thus, the term $\underline{p}^{(i)} \times [\underline{\underline{\xi}}^{(i)}]^{-1} \cdot \underline{T}_B^{(i)}(t)$ in Jeffrey's equation is given as

$$\begin{aligned} &\underline{p}^{(i)} \times [\underline{\underline{\xi}}^{(i)}]^{-1} \cdot \underline{T}_B^{(i)}(t) \\ &= \underline{p}^{(i)} \times \left(\frac{T_{B,\parallel}^{(i)}}{\xi_\parallel^{(i)}} \underline{p}^{(i)} + \frac{T_{B,\perp 1}^{(i)}}{\xi_{\perp 1}^{(i)}} \underline{p}_{\perp 1}^{(i)} + \frac{T_{B,\perp 2}^{(i)}}{\xi_{\perp 2}^{(i)}} \underline{p}_{\perp 2}^{(i)} \right) \\ &= \frac{T_{B,\perp 1}^{(i)}}{\xi_{\perp 1}^{(i)}} \underline{p}_{\perp 2}^{(i)} - \frac{T_{B,\perp 2}^{(i)}}{\xi_{\perp 2}^{(i)}} \underline{p}_{\perp 1}^{(i)} \end{aligned} \tag{B.34}$$

B.4. Brownian translational velocity and orientation

The effective velocity due to Brownian translational diffusion, $\underline{v}_B$, is given by

$$v_{B,x}^{(i)} = \frac{F_{B,\parallel}^{(i)}}{\zeta_\parallel^{(i)}} p_x^{(i)} + \frac{F_{B,\perp 1}^{(i)}}{\zeta_{\perp 1}^{(i)}} p_{\perp 1,x}^{(i)} + \frac{F_{B,\perp 2}^{(i)}}{\zeta_{\perp 2}^{(i)}} p_{\perp 2,x}^{(i)} \tag{B.35}$$

$$v_{B,y}^{(i)} = \frac{F_{B,\parallel}^{(i)}}{\zeta_{\parallel}^{(i)}} p_y^{(i)} + \frac{F_{B,\perp 1}^{(i)}}{\zeta_{\perp 1}^{(i)}} p_{\perp 1,y}^{(i)} + \frac{F_{B,\perp 2}^{(i)}}{\zeta_{\perp 2}^{(i)}} p_{\perp 2,y}^{(i)} \tag{B.36}$$

$$v_{B,z}^{(i)} = \frac{F_{B,\parallel}^{(i)}}{\zeta_{\parallel}^{(i)}} p_z^{(i)} + \frac{F_{B,\perp 1}^{(i)}}{\zeta_{\perp 1}^{(i)}} p_{\perp 1,z}^{(i)} + \frac{F_{B,\perp 2}^{(i)}}{\zeta_{\perp 2}^{(i)}} p_{\perp 2,z}^{(i)} \tag{B.37}$$

The effective rate of change due to Brownian rotational diffusion, $\underline{\dot{p}}_B$, is given by

$$\dot{p}_{B,x}^{(i)} = \frac{T_{B,\perp 2}^{(i)}}{\xi_{\perp 2}^{(i)}} p_{\perp 1,x}^{(i)} - \frac{T_{B,\perp 1}^{(i)}}{\xi_{\perp 1}^{(i)}} p_{\perp 2,x}^{(i)} \tag{B.38}$$

$$\dot{p}_{B,y}^{(i)} = \frac{T_{B,\perp 2}^{(i)}}{\xi_{\perp 2}^{(i)}} p_{\perp 1,y}^{(i)} - \frac{T_{B,\perp 1}^{(i)}}{\xi_{\perp 1}^{(i)}} p_{\perp 2,y}^{(i)} \tag{B.39}$$

$$\dot{p}_{B,z}^{(i)} = \frac{T_{B,\perp 2}^{(i)}}{\xi_{\perp 2}^{(i)}} p_{\perp 1,z}^{(i)} - \frac{T_{B,\perp 1}^{(i)}}{\xi_{\perp 1}^{(i)}} p_{\perp 2,z}^{(i)} \tag{B.40}$$

References

Chen, B.L., Selegue, J.P., 2002. Analytical Chemistry 74, 4774.
Chun, J., Fagan, J.A., Hobbie, E.K., Bauer, B.J., 2008. Analytical Chemistry 80, 2514.
Cobb, P.D., Butler, J.E., 2006. Macromolecules 39, 886.
Cobb, P.D., Byron, C., 2005. Journal of Chemical Physics 123 054908-054908-19.
Giddings, J.C., 1978. Separation Science and Technology 13, 241.
Giddings, J.C., 1993. Science 260, 1456.
Giddings, J.C., 2000. In: Field-Flow Fractionation Handbook (Chap. 1), Wiley-Interscience.
Giddings, J.C., Myers, M.N., 1978. Separation Science and Technology 13, 637.
Giddings, J.C., Moon, M.H., Williams, P.S., Myers, M.N., 1991. Analytical Chemistry 63, 1366.
Janca, J., 1987. In: Field-Flow Fractionation, Marcel Dekker, New York.
Jensen, K.D., Williams, S.K.R., Giddings, J.C., 1996. Journal of Chromatography A 746, 137.
Jiang, Y., Myers, M.N., Giddings, J.C., 1999. Journal of Liquid Chromatography & Related Technologies 22, 1213.
Kim, S. Karrila, S.J., 1991. In: Microhydrodynamics: Principles and Selected applications. Butterworth–Heinemann, Stoneham.
Liu, J., Rinzler, A.G., Dai, H.J., Hafner, J.H., Bradley, R.K., Boul, P.J., Lu, A., Iverson, T., Shelimov, K., Huffman, C.B., Rodriguez-Macias, F., Shon, Y.S., Lee, T.R., Colbert, D.T., Smalley, R.E., 1998. Science 280, 1253.
Moon, M.H., Kang, D.J., Jung, J.H., Kim, J.M., 2004. Journal of Separation Science 27, 710.
Peng, H.Q., et al., 2006. Journal of the American Chemical Society 128, 8396.
Perrin, F., 1936. Journal de Physique et le Radium 7, 1.
Phelan Jr., F.R., Bauer, B.J., 2007. Chemical Engineering Science 62, 4620.
Phelan Jr., F.R., Bauer, B.J., 2009. Chemical Engineering Communications, in preparation.
Satoh, A., 2003. In: Introduction to Molecular-Microsimulation of Colloidal Dispersions, Elsevier Science B.V., Amsterdam, The Netherlands.
Selegue, J.P., et al., 2001. Abstracts of Papers of the American Chemical Society 222 U524.
Song, J.H., Kim, W.S., Lee, D.W., 2003. Journal of Liquid Chromatography & Related Technologies 26, 3003.
Tagmatarchis, N., Zattoni, A., Reschiglian, P., Prato, M., 2005. Carbon 43, 1984.
Williams, P.S., Koch, T., Giddings, J.C., 1992. Chemical Engineering Communications 111, 121.
Williams, P.S., Lee, S.H., Giddings, J.C., 1994. Chemical Engineering Communications 130, 143.
Williams, P.S., Moon, M.H., Xu, Y.H., Giddings, J.C., 1996a. Chemical Engineering Science 51, 4477.
Williams, P.S., Moon, M.H., Giddings, J.C., 1996b. Colloids and Surfaces A-Physicochemical and Engineering Aspects 113, 215.
Williams, P.S., Xu, Y.H., Reschiglian, P., Giddings, J.C., 1997. Analytical Chemistry 69, 349.
Williams, P.S., Giddings, M.C., Giddings, J.C., 2001. Analytical Chemistry 73, 4202.
Zhang, J., Williams, P.S., Myers, M.N., Giddings, .J.C., 1994. Separation Science and Technology 29, 2493.
Zhang, L.X., Lin, J.Z., Chan, T.L., 2005. Physics of Fluids 17 093105-093105-8.